Three-qubit PHASE gate in lateral quantum dots: Influence of the acoustic phonon and quantum-dot configuration

Song Yang, Ming Gong, Chuanfeng Li, Cheng Zhao, Xubo Zou,[*] and Guangcan Guo

Key Laboratory of Quantum Information, University of Science and Technology of China, Hefei 230026, People's Republic of China

A one-step scheme is proposed to realize three-qubit controlled-PHASE (CPHASE) gate for electron spins in lateral quantum dots, and two different quantum-dot configurations (ring- and line-type) are considered. We investigate the effect of the acoustic phonon and spontaneous emission on the scheme. Numerical results show that the gate performance is primarily related to quantum-dot configuration and temperature, and can be significantly improved by selecting lower single-exciton resonance in line-type configuration.

I. INTRODUCTION

All-optical quantum computation using electron spins in quantum dots (QDs) seems particularly attractive in view of long decoherence time of spins ($\sim$ns) [1–3] and the high speed of optical transitions ($\sim$ps) [4]. With well developed technologies in semiconductors and lasers, initializing [5,6], manipulating [4] and detecting spin qubit [7] in a QD has been achieved experimentally. Although many two-qubit quantum operations, such as optical entanglement preparation [8,9] and controlled-phase gate [10,11], have been presented, very few multiqubit quantum gates in QD system [12] have been proposed so far. In fact, comparing with quantum networks consisting of many two-qubit gates and single qubit rotations, the multiqubit gate, which can reduce the number of quantum gates [13], is more efficient in constructing simpler and faster complicated quantum computation, such as quantum error correction [14] and Grover's search algorithm [15].

In this paper, we present an all-optical one-step scheme for realizing three-qubit controlled-phase gate on electron spins in lateral quantum dots. We investigate the effect of the acoustic phonon and spontaneous emission on the scheme. For three lateral QDs, there are two different coupling configurations: ring type and line type. We show that the factors, which affect the gate fidelity, mainly come from quantum-dot configuration and temperature. Furthermore, the gate quality can be significantly improved by selecting lower single-exciton resonance in line configuration. The study on multiple quantum gate in different configurations is of some practical reference values for complicated large scale quantum computing.

The structure of this paper is organized as follows. In Sec. II, we introduce the theoretical model based on quantum-dot system. In Sec. III, we explain the basic idea of implementing the three-qubit controlled-PHASE (CPHASE) gate via only one laser field, and also give the approximate analytical solution to the model. In Sec. IV, the effect of dissipation is discussed. To fully understand the scheme, in Sec. V, the numerical simulations to the model are presented to evaluate the influence of various phonon interactions, different con-

figurations, as well as anisotropy of quantum dot. Finally, our conclusion follows in Sec. VI.

II. MODEL

The systems studied in this paper are schematically shown in Figs. 1(a) and 1(b), where three quantum dots are arranged in ring- or line-type configuration, respectively. Each QD is doped with a single excess electron, and qubit bases are defined by electron spin states: $|m_z = \frac{1}{2}\rangle = |\uparrow\rangle$, and $|m_z = -\frac{1}{2}\rangle = |\downarrow\rangle$. Ideally, what we would like to realize is the three-qubit phase gate [16], which generates a π phase on one of the eight three-qubit computational basis states, while leaving the other seven states unchanged, i.e.,

$$U_p = \exp(i\pi \bigotimes_{j=1}^{3} |\uparrow_j\rangle\langle\uparrow_j|). \tag{1}$$

To perform such an operation, a σ^+ polarized laser with frequency ω_l is applied to drive the transition between spin state $|\uparrow\rangle$ and exciton state $|X_{\Uparrow}^+\rangle = |\uparrow\downarrow\Uparrow\rangle$, where $|X_{\Uparrow}^+\rangle$ is a positive charged trion state including an exciton (electron-hole pair) and a spin [see Fig. 1(c)]. The corresponding coupling strength is given by Ω. If a qubit is initialized at $|\downarrow\rangle$, no exciton will be created because of the Pauli blocking effect [10]. The Hamiltonian of system is given by $H = H_0 + H_{int}$, with

$$H_0 = \omega_x \sum_{i=1}^{3} n_i + V_F \sum_{\langle i,j \rangle} c_i^\dagger c_j + V_{xx} \sum_{\langle i,j \rangle} n_i n_j, \tag{2}$$
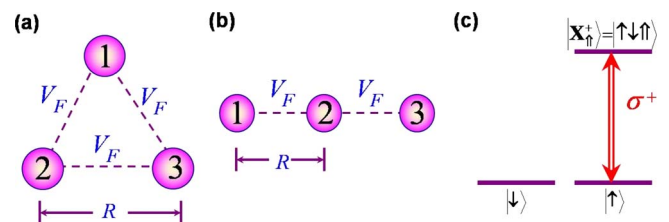

FIG. 1. (Color online) Possible configurations of three QDs system, ring configuration for (a) and line configuration for (b). The exciton energy level diagram due to Pauli blocking effect is illustrated in (c).
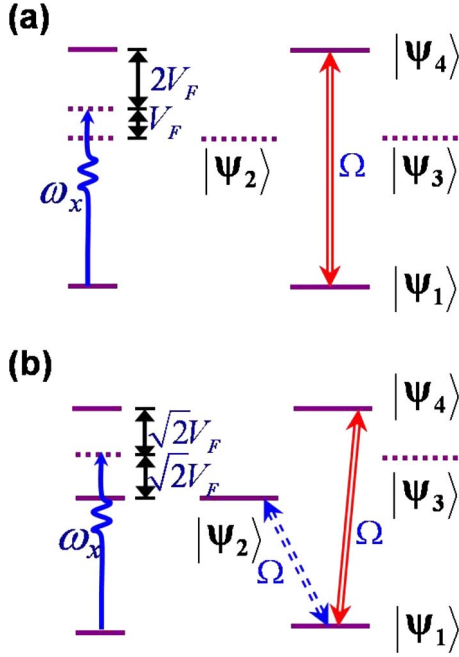
FIG. 2. (Color online) The energy level diagrams for ring and line configuration are shown in (a) and (b), respectively. The arrows represent the possible resonant transitions to implement the gate operation. The definition of $|\Psi_i\rangle$ can be found in the text.

$$H_{int} = \Omega \cos(\omega_l t) \sum_{i=1}^{3} (c_i^\dagger + c_i), \qquad (3)$$

where $c_i^\dagger = |X_\Uparrow^\dagger\rangle\langle\uparrow| $ $(c_i=|\uparrow\rangle\langle X_\Uparrow^\dagger|)$ is the creation (annihilation) operator of exciton at the ith QD, and we set $n_i = c_i^\dagger c_i$. The symbol $\langle i,j \rangle$ means that the sum is performed over the nearest neighbors only. ω_x is the exciton energy for each dot, V_F is the interdot Förster interaction strength [17], and V_{xx} is the bitrion energy shift. Förster interaction has been recently demonstrated by Kim *et al.* in semiconductor QDs [18].

Since the operator $\sum_{i=1}^{3}|\downarrow\rangle_i\langle\downarrow|$ commutes with the Hamiltonian (1) and is a conserved quantity, the Hamiltonian can be decoupled into four subspaces sorted by the number of qubit in the basis state $|\downarrow\rangle$. Additionally, with the help of Förster interaction V_F and static Coulomb interaction V_{xx}, the energy shift is different for each subspace. We pay attention to the subspace associated with the electron state $|\uparrow\uparrow\uparrow\rangle$. In this subspace, under the condition V_F, $V_{xx} \gg \Omega$, transitions from the initial state $|\uparrow\uparrow\uparrow\rangle$ to multitrion states can be effectively suppressed, and only the terms containing single trion need to be considered. In Fig. 2(a), we present the lowest four eigenstates of Eq. (2) in the ring-type configuration,

$$|\Psi_1\rangle = |\uparrow\uparrow\uparrow\rangle,$$

$$|\Psi_2\rangle = -\frac{1}{\sqrt{6}}(c_1^\dagger - 2c_2^\dagger + c_3^\dagger)|\uparrow\uparrow\uparrow\rangle,$$

$$|\Psi_3\rangle = \frac{\sqrt{2}}{2}(c_1^\dagger - c_3^\dagger)|\uparrow\uparrow\uparrow\rangle,$$

$$|\Psi_4\rangle = \frac{1}{\sqrt{3}}(c_1^\dagger + c_2^\dagger + c_3^\dagger)|\uparrow\uparrow\uparrow\rangle. \qquad (4)$$

Similarly, the lowest four eigenstates for the line-type configuration are shown in Fig. 2(b),

$$|\Psi_1\rangle = |\uparrow\uparrow\uparrow\rangle,$$

$$|\Psi_2\rangle = \frac{1}{2}(c_1^\dagger - \sqrt{2}c_2^\dagger + c_3^\dagger)|\uparrow\uparrow\uparrow\rangle,$$

$$|\Psi_3\rangle = -\frac{\sqrt{2}}{2}(c_1^\dagger - c_3^\dagger)|\uparrow\uparrow\uparrow\rangle,$$

$$|\Psi_4\rangle = \frac{1}{2}(c_1^\dagger + \sqrt{2}c_2^\dagger + c_3^\dagger)|\uparrow\uparrow\uparrow\rangle. \qquad (5)$$

III. ONE-STEP THREE-QUBIT CPHASE GATE

In this section, we develop an analytical model for one-step implementation of the three-qubit phase gate. In general, the implementation of the three-qubit phase gate requires a lot of two-qubit controlled gates and one-qubit rotations [13]. However, we will show that such a gate can be realized via only one step operation. For this purpose, we tune the laser frequency so that the initial state $|\Psi_1\rangle$ interacts resonantly with $|\Psi_s\rangle$, which is one of the single-exciton dressed states (shown in Fig. 2). Under the condition V_F, $V_{xx} \gg \Omega$, the laser field is far off the resonance with undesirable transitions, and the effective Hamiltonian can be given by

$$H_{\mathrm{eff}} = \frac{\alpha\Omega(t)}{2}(|\Psi_s\rangle\langle\uparrow\uparrow\uparrow| + \mathrm{H.c.}), \qquad (6)$$

where α is character factor, which is determined by quantum-dot configuration. For ring-type configuration, $\alpha=\sqrt{3}$, $|\Psi_s\rangle=|\Psi_4\rangle$, but for line configuration, there exist two cases: (i) high exciton energy level, $\alpha=1+\frac{\sqrt{2}}{2}$, $|\Psi_s\rangle=|\Psi_4\rangle$; (ii) low exciton energy level, $\alpha=1-\frac{\sqrt{2}}{2}$, $|\Psi_s\rangle=|\Psi_2\rangle$. Hence the time evolution of the initial state $|\uparrow\uparrow\uparrow\rangle$ has the following form:

$$|\uparrow\uparrow\uparrow\rangle \rightarrow \cos\theta(t)|\uparrow\uparrow\uparrow\rangle + ie^{-i\omega_l t}\sin\theta(t)|\Psi_s\rangle, \qquad (7)$$

with $\theta(t)=\frac{\alpha}{2}\int_0^t d\tau\Omega(\tau)$. If we choose the interaction time T for $\theta(T)=\pi$, the state $|\uparrow\uparrow\uparrow\rangle$ will acquire a π phase, i.e.,

$$|\uparrow\uparrow\uparrow\rangle \rightarrow -|\uparrow\uparrow\uparrow\rangle. \qquad (8)$$

For the weak coupling strength, the polarized laser field cannot induce any transitions in other three subspaces which are associated with the number of qubits $|\downarrow\rangle$, and only the state $|\uparrow\uparrow\uparrow\rangle$ experiences dynamic evolution. Thus, the three-qubit phase gate is achieved only in need of one laser field to couple the three qubits collectively [10,11]. Moreover, this one-step scheme does not require laser addressing of individual quantum dot, and may be of much more feasibility with current experimental technology.

To implement the control gate, we should designate the control and target qubits in our scheme. From the perspective

of geometric symmetry, the three qubits are of equal status in the ring type, therefore one can choose any qubit to be target qubit, and the other two qubits to be control qubits. For the line type, the central qubit is different from the other two end qubits, so we can select one of the end qubits to be target qubit. For example, we set qubits 1 and 2 as control qubits, and set qubit 3 as target qubit [illustrated in Figs. 1(a) and 1(b)].

The three-qubit phase gate can be used to generate entanglement. To characterize and quantify the entanglement of three-qubit state, we can use the measure of the three tangle τ_{123} [19]. If the input state is $|\Psi_{in}\rangle=[\frac{1}{\sqrt{2}}(|\uparrow\rangle+|\downarrow\rangle)]^{\otimes 3}$, the output state of this three-qubit phase gate will be $|\Psi_{out}\rangle=[\frac{1}{\sqrt{2}}(|\uparrow\rangle+|\downarrow\rangle)]^{\otimes 3}-2|\uparrow\uparrow\uparrow\rangle$. We can find that the input state is a separable state with $\tau_{123}=0$, while the output state is an entangled state with $\tau_{123}=0.5$. The nonlocal property of the three-qubit phase gate is testified.

It should also be noted that the dots in practice always have energies which are not the same, and the energy difference is at least hundreds of μeV. Take the ring configuration for example. We suppose that the energy of single exciton in one dot is different from the other two dots by δ. Without loss of generality, we assume the single-exciton energies for both QD1 and QD3 are ω_x, while energy for QD2 is $\omega_x+\delta$. The three single-exciton eigenvectors in the subspace associated with $|\uparrow\uparrow\uparrow\rangle$ are

$$|\Psi_2\rangle=-\mathcal{A}_2\left(c_1^\dagger+\frac{3V_F+B}{3V_F-A}c_2^\dagger+c_3^\dagger\right)|\uparrow\uparrow\uparrow\rangle,$$

$$|\Psi_3\rangle=\frac{\sqrt{2}}{2}(c_1^\dagger-c_3^\dagger)|\uparrow\uparrow\uparrow\rangle,$$

$$|\Psi_4\rangle=-\mathcal{A}_4\left(c_1^\dagger+\frac{3V_F+A}{3V_F-B}c_2^\dagger+c_3^\dagger\right)|\uparrow\uparrow\uparrow\rangle, \quad (9)$$

with $A=\delta+\sqrt{8V_F^2+(V_F-\delta)^2}$, $B=\delta-\sqrt{8V_F^2+(V_F-\delta)^2}$. In above equations, $\mathcal{A}_i$ represents the normalization factor of $|\Psi_i\rangle$. And those corresponding energies are

$$E_2=\omega_0+\frac{V_F+B}{2},$$

$$E_3=\omega_0-V_F,$$

$$E_4=\omega_0+\frac{V_F+A}{2}. \quad (10)$$

We still choose $|\Psi_s\rangle=|\Psi_4\rangle$, and $\alpha=\sqrt{9V_F-\delta+3\sqrt{8V_F^2+(V_F-\delta)^2}}/\{\sqrt{2}[8V_F^2+(V_F-\delta)^2]^{1/4}\}$. When $\delta=0$, the result reduces to the special case where three dots are resonant. However, as the energy difference $|\delta|$ increases, the minimum energy difference between $|\Psi_4\rangle$ and all other single-exciton states decreases. This adds more challenges for us to select the transition $|\Psi_1\rangle\leftrightarrow|\Psi_4\rangle$ without driving other unwanted transitions. Another effect is that the operation time for three-qubit gate is prolonged. To this end, we had better control the value $|\delta|$ within ~ 500 μeV to guarantee the good performance of three-qubit gate. There are some

techniques, such as applying external electric field [20] and annealing [21,22], which can tune the exciton energies of dots in order to fabricate resonant or near-resonant QDs.

IV. DECOHERENCE DUE TO ENVIRONMENT AND CONFIGURATION EFFECTS

To explore the CPHASE performance in an open mesoscopic system which is embedded in both phonon environment and radiation field, we derive a full master equation including various dissipation sources to describe the dynamic evolution. Here we focus on the low temperature regime, and consider the influence of the acoustic phonons. The exciton-phonon interaction [23] can be written as

$$H_{ep}=\sum_{j=1}^3\sum_{\mathbf{q}}g_{q,j}c_j^\dagger c_j(a_{\mathbf{q}}+a_{\mathbf{q}}^\dagger), \quad (11)$$

with the effective excitonic coupling strength

$$g_{\mathbf{q},j}=e^{i\mathbf{q}\cdot\mathbf{d_j}}[M_{q,j}^e\rho_e(\mathbf{q})-M_{q,j}^h\rho_h(\mathbf{q})], \quad (12)$$

in which

$$\rho_{e(h)}(\mathbf{q})=\int d^3r|\phi_{e(h)}|^2e^{i\mathbf{q}\cdot\mathbf{r}}, \quad (13)$$

is the form factor and $M_{q,j}^{e(h)}$ denotes the bulk coupling matrix element. $a_{\mathbf{q}}(a_{\mathbf{q}}^\dagger)$ is the annihilation (creation) operator for phonon with wave vector $\mathbf{q}$. $\mathbf{d_j}$ represents the location of QDs, which is determined by the configuration. The wave function we choose is $\phi_{e(h)}\sim\exp(-r^2/2l_{e(h)}^2)$, with $l_{e(h)}$ denoting the electron (hole) localization length.

Since the interaction between acoustic phonons and excitons may be mediated by deformation potential coupling and piezoelectric coupling, the bulk coupling matrix element $M_{q,j}^{e(h)}$ is given by [23]

$$M_{q,j}^{e(h)}=\sum_{\mathbf{q}}\sqrt{\frac{\hbar}{2\mu|q|Vc_s}}(|q|D_{e(h)}+iP_{\mathbf{q}}), \quad (14)$$

in which μ denotes the mass density, V the normalization volume, c_s the sound velocity of the phonon, and $|q|=\frac{\omega}{c_s}$ the modulus of $\mathbf{q}$. $D_{e(h)}$ is the deformation potential coupling constant of electron (hole) which is zero except for the longitudinal-acoustic (LA) mode. $P_{\mathbf{q}}$ is the piezoelectric coupling which arises from both longitudinal-acoustic mode and transverse-acoustic (TA) mode [24],

$$P_{\mathbf{q}}=-\sum_{\mathbf{q}}\frac{8\pi ee_{14}}{\epsilon_0\epsilon_s|q|^2}(\eta_xq_yq_z+\eta_yq_zq_x+\eta_zq_xq_y), \quad (15)$$

with

$$\vec{\eta}(\text{LA})=(\sin\theta\cos\varphi,\sin\theta\sin\varphi,\cos\theta),$$

$$\vec{\eta}(\text{TA1})=(\sin\varphi,-\cos\varphi,0),$$

$$\vec{\eta}(\text{TA2})=(-\cos\theta\cos\varphi,-\cos\theta\sin\varphi,\sin\theta), \quad (16)$$

where ϵ_0 and ϵ_s are the vacuum permittivity and the static dielectric constants, respectively.

Following the Markov approximation, the master equation for the density matrix of the whole system may be reduced to a Lindblad form

$$\dot{\rho} = -i[H,\rho] + \sum_i J(\omega_i)\{[N(\omega_i)+1]D[L_i]\rho + N(\omega_i)D[L_i^\dagger]\rho\},$$

$$(17)$$

where

$$D[L]\rho = L\rho L^\dagger - \frac{1}{2}(L^\dagger L\rho + \rho L^\dagger L) \qquad (18)$$

is the decay operator of phonon effect, and $N(\omega) = [\exp(\omega/k_B T) - 1]^{-1}$ is the thermal occupation of the phonon modes. $J(\omega)$ denotes the phonon spectral density, which depends strongly on the configuration. We set $\mathbb{G}_d(\omega)$ as the common factor of deformation potential effect, $\mathbb{G}_p(\omega)$ as the common factor of piezoelectric potential effect, $f_p(\theta,\varphi)$ as the factor of three kinds of phonon modes, and $J_c(\omega)$ as the factor of configuration effect in spectral densities. The spectral density $J(\omega)$ is calculated as

$$J(\omega) = \int d\Omega J_c(\omega)[\mathbb{G}_d(\omega) + \mathbb{G}_p(\omega)f_p(\theta,\varphi)], \qquad (19)$$

with

$$\mathbb{G}_d(\omega) = \frac{\omega^3}{8\pi^2\mu c_s^5}[D_e e^{-(\omega l_e/2c_s)^2} - D_h e^{-(\omega l_h/2c_s)^2}]^2,$$

$$\mathbb{G}_p(\omega) = \frac{8e^2\omega e_{14}^2}{\epsilon_0^2\epsilon_s^2\mu c_s^3}[e^{-(\omega l_e/2c_s)^2} - e^{-(\omega l_h/2c_s)^2}]^2,$$

$$f_p(\theta,\varphi) = \frac{1}{32}\sin^2\theta[18 + 14\cos 2\theta + \cos(2\theta - 4\varphi)$$

$$- 2\cos(4\varphi) + \cos(2\theta + 4\varphi)]. \qquad (20)$$

In the case of the ring configuration, the Hamiltonian of the total system (acoustic phonon and quantum dots) follows:

$$H = H'_{sub} + \sum_q \omega_q a_q^\dagger a_q + H_{ep}, \qquad (21)$$

where H'_{sub} describes the transitions between the dressed states shown in Fig. 2(a),

$$H'_{sub} = -3V_F|\Psi_2\rangle\langle\Psi_2| - 3V_F|\Psi_3\rangle\langle\Psi_3|$$

$$+ \frac{\sqrt{3}\Omega}{2}(|\Psi_1\rangle\langle\Psi_4| + \text{H.c.}). \qquad (22)$$

Following approaches mentioned in [25], we move the Hamiltonian into the interaction picture with respect to $H'_{sub} + \sum_q \omega_q a_q^\dagger a_q$, and calculate the spectral densities $J(\omega)$. The relevant parameters are shown in Table I. The states $|\Phi_1\rangle$, $|\Psi_2\rangle$, $|\Psi_3\rangle$, and $|\Phi_4\rangle$ are the eigenstates of H'_{sub}, with $|\Phi_1\rangle = \frac{1}{\sqrt{2}}(|\Psi_1\rangle - |\Psi_4\rangle)$ and $|\Phi_4\rangle = \frac{1}{\sqrt{2}}(|\Psi_1\rangle + |\Psi_4\rangle)$.

The analysis of the line configuration can be derived in analogy to the ring configuration. As shown in Fig. 2(b), both

TABLE I. Configuration factors of spectral density with different frequencies and dissipative operators in ring configuration. The character factor $\alpha = \sqrt{3}$ [in Eq. (6)] and $d = R/\sqrt{3}$.

$J_c(\omega)$	L	ω
$2 - 2\cos(\sqrt{3}|q|d\sin\theta\sin\varphi)$	$\frac{1}{2\sqrt{3}}|\Psi_2\rangle\langle\Phi_4|$	$3V_F + \frac{1}{2}\alpha\Omega$
	$\frac{1}{2\sqrt{3}}|\Psi_2\rangle\langle\Phi_1|$	$3V_F - \frac{1}{2}\alpha\Omega$
$9\sin^2\theta\cos^2\varphi|q|^2d^2 -$	$\frac{1}{6}|\Psi_3\rangle\langle\Phi_4|$	$3V_F + \frac{1}{2}\alpha\Omega$
$\frac{9}{32}\sin^4\theta(3 + \cos 2\varphi - \cos 4\varphi)|q|^4d^4$	$\frac{1}{6}|\Psi_3\rangle\langle\Phi_1|$	$3V_F - \frac{1}{2}\alpha\Omega$
$9 - \frac{9}{2}\sin^2\theta|q|^2d^2 + \frac{27}{32}\sin^4\theta|q|^4d^4$	$\frac{1}{6}|\Phi_1\rangle\langle\Phi_4|$	$\alpha\Omega$

$|\Psi_2\rangle$ and $|\Psi_4\rangle$ have an energy shift from ω_x, and can be resonantly coupled to the level $|\Psi_1\rangle$. Then we obtain spectral densities $J(\omega)$ in two different resonant transitions: one is from ground state $|\Phi_1\rangle$ to low exciton energy level $|\Psi_2\rangle$, and the other is from $|\Phi_1\rangle$ to high exciton energy level $|\Psi_4\rangle$. The corresponding results are listed in Table II. For convenience, we label two new eigenvectors as $|\Phi_1\rangle = \frac{1}{\sqrt{2}}(|\Psi_1\rangle - |\Psi_s\rangle)$, $|\Phi_s\rangle = \frac{1}{\sqrt{2}}(|\Psi_1\rangle + |\Psi_s\rangle)$ $(s = 2, 4)$.

So far, we have only considered the influence of acoustic phonon on the system. Nevertheless, the finite exciton lifetime might also affect the gate operation. This can be taken into account by adding the spontaneous emission terms (with decay rate Γ)

$$R[\rho] = \sum_{i=1}^3 \Gamma\left[c_i\rho c_i^\dagger - \frac{1}{2}(c_i^\dagger c_i\rho + \rho c_i^\dagger c_i)\right] \qquad (23)$$

to the right side of the density operator master equation Eq. (17).

V. DISCUSSION AND NUMERICAL SIMULATIONS

In the preceding sections, we present the theoretical model and basic formulations. Now for a more concrete calculation, we will compare the effects of two phonon interactions, then discuss the anisotropic effect of the QD, and finally give an exact solution to the system dynamics through numerical simulations. Here we consider the prototype InAs/GaAs QDs, and choose the parameters $V_F = 0.85$ meV, exci-

TABLE II. Configuration factors of spectral density with different frequencies and dissipative operators in line configuration. The character factor $\alpha = 1 + \frac{\sqrt{2}}{2}$ for transition between $|\Psi_1\rangle$ and $|\Psi_4\rangle$, and $\alpha = 1 - \frac{\sqrt{2}}{2}$ for transition between $|\Psi_1\rangle$ and $|\Psi_2\rangle$. Here we set $d = R$ in the line configuration.

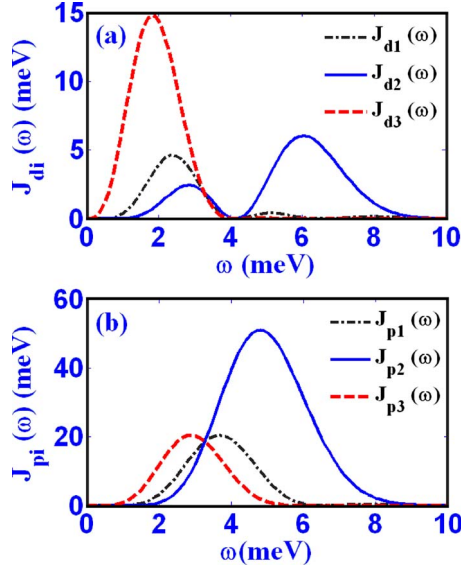| $J_c(\omega)$	$L_{\text{low-level}}$	$L_{\text{high-level}}$	ω
$4\sin^2(|q|d\cos\theta)$	$\frac{1}{4}|\Phi_1\rangle\langle\Psi_3|$	$\frac{1}{4}|\Psi_3\rangle\langle\Phi_4|$	$\sqrt{2}V_F + \frac{1}{2}\alpha\Omega$
	$\frac{1}{2\sqrt{2}}|\Psi_3\rangle\langle\Psi_4|$	$\frac{1}{2\sqrt{2}}|\Psi_2\rangle\langle\Psi_3|$	$\sqrt{2}V_F$
	$\frac{1}{4}|\Phi_2\rangle\langle\Psi_3|$	$\frac{1}{4}|\Psi_3\rangle\langle\Phi_1|$	$\sqrt{2}V_F - \frac{1}{2}\alpha\Omega$
$16\sin^4(\frac{|q|d\cos\theta}{2})$	$\frac{1}{4\sqrt{2}}|\Phi_1\rangle\langle\Psi_4|$	$\frac{1}{4\sqrt{2}}|\Psi_2\rangle\langle\Phi_4|$	$2\sqrt{2}V_F + \frac{1}{2}\alpha\Omega$
	$\frac{1}{4\sqrt{2}}|\Phi_2\rangle\langle\Psi_4|$	$\frac{1}{4\sqrt{2}}|\Psi_2\rangle\langle\Phi_1|$	$2\sqrt{2}V_F - \frac{1}{2}\alpha\Omega$
$16\cos^4(\frac{|q|d\cos\theta}{2})$	$\frac{1}{8}|\Phi_1\rangle\langle\Phi_2|$	$\frac{1}{8}|\Phi_1\rangle\langle\Phi_4|$	$\alpha\Omega$

FIG. 3. (Color online) The spectral densities of line configuration: (a) for deformation potential interaction, (b) for piezoelectric interaction. All the three spectral densities of $J_{di}(\omega)$ or $J_{pi}(\omega)$ corresponding to $J_c(\omega)$ listed in Table II: $J_{d(p)1}(\omega)$, $J_{d(p)2}(\omega)$, and $J_3(\omega)$ are relevant to $J_{c1}(\omega) = 4 \sin^2(|q|d \cos \theta)$, $J_{c2}(\omega) = 16 \sin^4(\frac{|q|d \cos \theta}{2})$ and $J_{c3}(\omega) = 16 \cos^4(\frac{|q|d \cos \theta}{2})$, respectively.

ton energy $\omega_x = 1.1$ eV, bi-trion binding energy $V_{xx} = 3$ meV, Rabi frequency of external laser field $\Omega = 0.1$ meV, radiative decay rate $\Gamma = 1.6$ μeV, distance between adjacent QDs $R = 3.5$ nm [25], electron and hole ground state localization length $l_e = 2.16$ nm, $l_h = 1.44$ nm, mass density $\mu = 5.3$ g/cm^3, and the sound velocity $c_s = 4.8 \times 10^5$ cm/s. We set deformation potential coupling constant as $D_e = -14.6$ eV and $D_h = -4.8$ eV, piezoelectric constant as $e_{14} = 0.16$ C/m^2, static dielectric constant as $\varepsilon_s = 12.56$ [23].

A. Exciton-phonon interaction

In the above calculations, we introduce two kinds of exciton-phonon interaction: deformation potential interaction and piezoelectric interaction. For two-qubit case [11], the decay rate due to deformation potential interaction is one order of magnitude larger than that due to piezoelectric interaction. Thus the deformation potential coupling due to LA phonons might be considered to be the dominant phonon decoherence mechanism, while the piezoelectric coupling can be neglected. For three-qubit case, we take the spectral functions of line configuration for example. As shown in Fig. 3, the spectral density of piezoelectric coupling J_p is comparable to that of deformation potential coupling J_d. Therefore, piezoelectric decoherence cannot be ignored. We also find that the deformation potential coupling remains the primary decoherence mechanism in the region $\omega \lesssim 3$ meV.

B. Effect of anisotropic quantum dot

In the theoretical analysis above, we have assumed that the wave function of QD is isotropic, which indicates that the
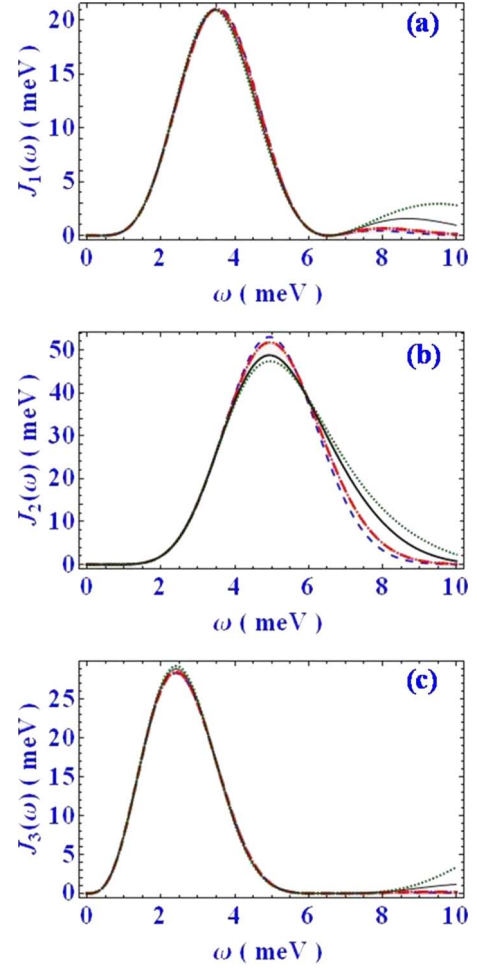

FIG. 4. (Color online) Comparisons of spectral densities in different wave function model. The spectral densities $J_i(\omega)$ correspond to $J_c(\omega)$ which are listed in Table II: $J_1(\omega)$ in (a), $J_2(\omega)$ in (b) and $J_3(\omega)$ in (c) are relevant to $J_{c1}(\omega) = 4 \sin^2(|q|d \cos \theta)$, $J_{c2}(\omega) = 16 \sin^4(\frac{|q|d \cos \theta}{2})$ and $J_{c3}(\omega) = 16 \cos^4(\frac{|q|d \cos \theta}{2})$, respectively. The four curves in each figure describe the relationship between the spectral density and frequencies under different wave functions: isotropy in which the offsets are $\xi_{e(h)} = 0$ (blue, dashed line), cylindrical symmetry with the offsets $\xi_{e(h)} = 0.1$ (red, dash-dot line), $\xi_{e(h)} = 0.2$ (black, solid line), as well as $\xi_{e(h)} = 0.3$ (green, dotted line).

electron (hole) localization length has tantamount value as $l_{e(h)}$ in all directions. But the wave function $\phi_{e(h)}$ of real QD might in principle be anisotropic, which typically exhibits cylindrical symmetry, and can be expressed as $\phi_{e(h)} \sim \exp\{-\frac{1}{2}[\frac{x^2+y^2}{l^2_{\|e(h)}} + (\frac{z}{l_{ze(h)}})^2]\}$. However, we find that the spectral densities generated from both the isotropic and anisotropic wave functions are in good agreement within the low-frequency regime (≤ 3 meV). The numerical results of three kinds of spectral densities $J_i(\omega)$ in the line configuration are shown in Fig. 4. The blue dashed lines show the isotropic case that $l_e = 2.16$ nm and $l_h = 1.44$ nm. Since a real QD is of flat and cylindrical symmetric shape, the transverse component $l_{\|e(h)}$ is larger than the longitudinal axis component $l_{ze(h)}$. We use $\xi_{e(h)}$ to describe the offset ratio of

localization length which represents the anisotropy of QD. Thus in-plane component $l_{\|e(h)}$ and the longitudinal component $l_{ze(h)}$ of localization length can be written as

$$l_{\|e(h)} = l_{e(h)}(1 + \xi_{e(h)}),$$

$$l_{ze(h)} = l_{e(h)}(1 - 2\xi_{e(h)}). \tag{24}$$

We discuss the anisotropy cases ($\xi_{e(h)} \neq 0$) and choose three offsets: (i) $\xi_{e(h)} = 0.1$, (ii) $\xi_{e(h)} = 0.2$, and (iii) $\xi_{e(h)} = 0.3$. The larger the offset is, the more obvious the anisotropy will be. From the simulation results illustrated in Fig. 4, we find that in the low-frequency limit, the isotropic wave function model is representative and the spectral density does not change a lot when the wave function becomes anisotropic.

C. Fidelity of three-qubit CPHASE gate

In order to check effects of acoustic phonon and spontaneous emission on our scheme, we give numerical calculations on the ring- and line-type system via the full master equation. In Fig. 5, we plot the fidelity $\mathcal{F} = |\langle \Psi_{in}|U_p^\dagger \rho(t) U_p|\Psi_{in}\rangle|$ of state created from the initial state $|\Psi_{in}\rangle = [\frac{1}{\sqrt{2}}(|\uparrow\rangle + |\downarrow\rangle)]^{\otimes 3}$, where $\rho(t)$ is time-dependent density operator and U_p is three-qubit phase gate $U_p = \exp(i\pi \otimes_{j=1}^3 |\uparrow_j\rangle\langle\uparrow_j|)$.

The fidelity of the ring configuration is illustrated in Fig. 5(a). The black solid line is the result when no dissipation is considered, and shows perfect Rabi oscillations. We may find that spontaneous radiation is not a primary decoherence source, since its contribution is so small that Rabi oscillations can preserve for a long time. Furthermore, the decoherence due to phonon-exciton interaction, which includes both deformation potential and piezoelectric coupling, can be considered as the dominant decay source. The fidelity is shown to be quickly damped, and no clear oscillations are observable even if the temperature achieves its limit $T = 0$ K. As T increases, the system suffers a stronger damping, and oscillations rapidly disappear after one period (~ 50 ps).

The numerical simulations of line configuration including all four levels are presented in Fig. 5(b) for high-level and Fig. 5(c) for low-level case. For the high-level case, though the maximum fidelity is a little higher, the behavior is similar to the one in the ring configuration that Rabi oscillations are damped quickly when phonon effect exists. This is because both cases share a similar character factor of configuration. For the low-level case, the gate has a longer oscillation period because it has the smaller character factor than the other two cases. Moreover, this level is the ground state of the system and does not suffer severe decoherence as the other two cases. Therefore, the gate here becomes more insensitive to temperature, and phonon effect does not result in a strong damping at very low temperature. Especially at 0 K, the behavior is as the same as that when only the spontaneous radiation is considered. As the temperature increases, oscillations are damped: for $T = 5$ K, two periods of Rabi oscillations are still visible, but no clear oscillations are exhibited for $T = 10$ K. This enables us to perform a CPHASE gate below $T = 5$ K with fidelity beyond 94.7%, which is much larger than the other two cases.
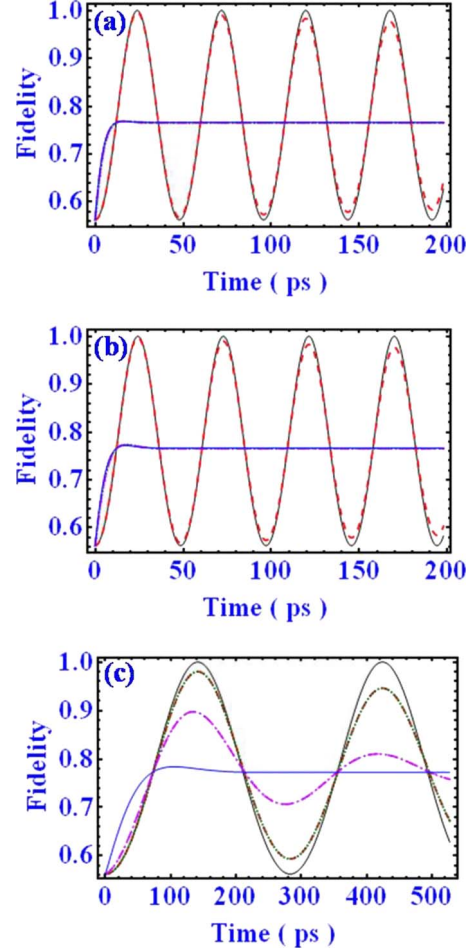

FIG. 5. (Color online) The fidelity as a function of time with $\Omega = 0.1$ meV and $R = 3.5$ nm: (a) for ring configuration, (b) for line configuration with transition $|\Psi_1\rangle \leftrightarrow |\Psi_4\rangle$, (c) for line configuration with transition $|\Psi_1\rangle \leftrightarrow |\Psi_2\rangle$. We present five curves in each figure to describe the performance of CPHASE gate in different conditions: without noise (black, solid line), only spontaneous radiation (red, dashed line), combining both spontaneous and phonon effects at three finite temperature. Temperature T varies from $T = 0$ K (green, dotted line), 5 K (pink, dash-dot line), 10 K (blue, solid line).

To further emphasize the effect of anisotropic quantum dot and the role of piezoelectric interaction in decoherence mechanism, we study the fidelity of the CPHASE gate in corresponding occasions. We consider the low-level case of the line configuration, and fix the temperature $T = 5$ K. In Fig. 6, we compare the gate fidelities of different offset rations $\xi_{e(h)}$, then find that those anisotropic cases are in good agreement with the isotropic case. It confirms that the anisotropy of electron (hole) does not have a strong impact on the behavior of three-qubit gate. As shown in Fig. 7, the fidelity of the phase gate can, respectively, achieve 97.3%, 95.3%, or 94.7%, when piezoelectric, deformation potential, or both coupling is considered. It infers that at $T = 5$ K, the gate fidelity is reduced by 0.6% because of the piezoelectric coupling, while the fidelity decreases by 2.6% for the deformation potential interaction.
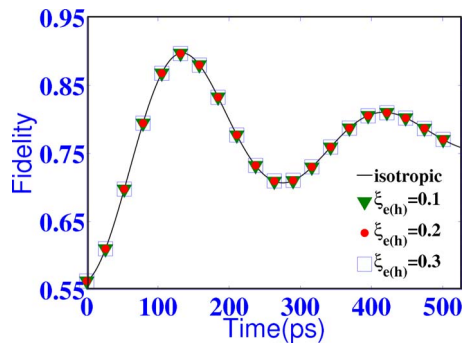
FIG. 6. (Color online) The comparison of three-qubit CPHASE gate fidelity in isotropic and anisotropic wave function model: isotropic (black, solid line), $\xi_{e(h)}=0.1$ (green ▼), $\xi_{e(h)}=0.2$ (red ●), as well as $\xi_{e(h)}=0.3$ (blue, □).
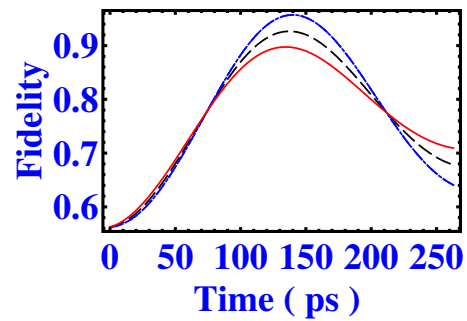

FIG. 7. (Color online) The influence of exciton-phonon interaction on three-qubit CPHASE gate fidelity: only the deformation potential coupling (black, dashed line), only the piezoelectric coupling (blue dash-dot line), and both the deformation potential and piezoelectric coupling (red, solid line).

VI. CONCLUSION

In summary, we have studied the configuration effect on the one-step CPHASE gate via modifying energy level structure and phonon-exciton coupling strength. By comparing the fidelity between ring and line configuration, we show that the gate fidelity is primarily related to QD configuration and temperature, and the gate quality can be significantly improved by selecting lower single-exciton resonance in line-type configuration. Our work will permit a detailed experimental investigation in arrangement of QD arrays and in fabrication of complicated quantum information processing.

[1] A. Greilich, D. R. Yakovlev, A. Shabaev, Al. L. Efros, I. A. Yugova, R. Oulton, V. Stavarache, D. Reuter, A. Wieck, and M. Bayer, Science **313**, 341 (2006).

[2] M. V. Gurudev Dutt, J. Cheng, B. Li, X. Xu, X. Li, P. R. Berman, D. G. Steel, A. S. Bracker, D. Gammon, S. E. Economou, R.-B. Liu, and L. J. Sham, Phys. Rev. Lett. **94**, 227403 (2005).

[3] P.-F. Braun *et al.*, Phys. Rev. Lett. **94**, 116601 (2005).

[4] J. Berezovsky, M. H. Mikkelsen, N. G. Stoltz, L. A. Coldren, and D. D. Awschalom, Science **320**, 349 (2008).

[5] M. Atatüre, J. Dreiser, A. Badolato, A. Högele, K. Karrai, and A. Imamoglu, Science **312**, 551 (2006).

[6] C. Emary, X. Xu, D. G. Steel, S. Saikin, and L. J. Sham, Phys. Rev. Lett. **98**, 047401 (2007).

[7] M. H. Mikkelsen, J. Berezovsky, N. G. Stoltz, L. A. Coldren, and D. D. Awschalom, Nat. Phys. **3**, 770 (2007).

[8] S. K. Saikin, C. Emary, D. G. Steel, and L. J. Sham, Phys. Rev. B **78**, 235314 (2008).

[9] C. Piermarocchi, Pochung Chen, L. J. Sham, and D. G. Steel, Phys. Rev. Lett. **89**, 167402 (2002).

[10] A. Nazir, B. W. Lovett, S. D. Barrett, T. P. Spiller, and G. A. D. Briggs, Phys. Rev. Lett. **93**, 150502 (2004).

[11] Erik M. Gauger, Ahsan Nazir, Simon C. Benjamin, Thomas M. Stace, and Brendon W. Lovett, New J. Phys. **10**, 073016 (2008).

[12] Bi Qiao, H. E. Ruda *et al.*, J. Appl. Phys. **91**, 2524 (2002).

[13] Z. Diao, M. S. Zubairy, and G. Chen, Z. Naturforsch., A: Phys. Sci. **57(a)**, 701 (2002).

[14] J. Chiaverini *et al.*, Nature (London) **432**, 602 (2004).

[15] M. S. Zubairy, A. B. Matsko, and M. O. Scully, Phys. Rev. A **65**, 043804 (2002).

[16] M. A. Nielsen and I. L. Chuang, *Quantum Computation and Quantum Information* (Cambridge University Press, Cambridge, England, 2000).

[17] K. Heldmann, W. G. Teich, and G. Mahler, Phys. Rev. B **44**, 3829 (1991).

[18] D. G. Kim, S. Okahara, M. Nakayama, and Y. G. Shim, Phys. Rev. B **78**, 153301 (2008).

[19] V. Coffman, J. Kundu, and W. K. Wootters, Phys. Rev. A **61**, 052306 (2000).

[20] A. Nazir, B. W. Lovett, S. D. Barrett, J. H. Reina, and G. A. Briggs, Phys. Rev. B **71**, 045334 (2005).

[21] S. Malik and C. Roberts *et al.*, Appl. Phys. Lett. **71**, 1987 (1997).

[22] R. J. Young and R. M. Stevenson *et al.*, Physica E **32**, 97 (2006).

[23] B. Krummheuer, V. M. Axt, and T. Kuhn, Phys. Rev. B **65**, 195313 (2002).

[24] T. Takagahara, Phys. Rev. B **60**, 2638 (1999).

[25] E. M. Gauger, S. C. Benjamin, A. Nazir, and B. W. Lovett, Phys. Rev. B **77**, 115322 (2008).